Energy exchange dynamics across L–H transitions in NSTX

2017 Nucl. Fusion 57 066050

(http://iopscience.iop.org/0029-5515/57/6/066050)

IOP Publishing | International Atomic Energy Agency Nuclear Fusion

Nucl. Fusion **57** (2017) 066050 (12pp) https://doi.org/10.1088/1741-4326/aa6a24

Energy exchange dynamics across L–H transitions in NSTX

A. Diallo[1], S. Banerjee[2], S.J. Zweben[1] and T. Stoltzfus-Dueck[1]

[1] Princeton Plasma Physics Laboratory, Princeton University, NJ, United States of America
[2] Institute for Plasma Research, Bhat, Gandhinagar 382428, Gujarat, India

E-mail: adiallo@pppl.gov

Received 14 November 2016, revised 27 February 2017
Accepted for publication 30 March 2017
Published 10 May 2017

Abstract

We studied the energy exchange dynamics across the low-to-high-confinement (L–H) transition in NSTX discharges using the gas-puff imaging (GPI) diagnostic. The investigation focused on the energy exchange between flows and turbulence to help clarify the mechanism of the L–H transition. We applied this study to three types of heating schemes, including a total of 17 shots from the NSTX 2010 campaign run. Results show that the edge fluctuation characteristics (fluctuation levels, radial and poloidal correlation lengths) measured using GPI do not vary just prior to the H-mode transition, but change after the transition. Using a velocimetry approach (orthogonal-dynamics programming), velocity fields of a 24×30 cm GPI view during the L–H transition were obtained with good spatial ($\sim$1 cm) and temporal ($\sim$2.5 μs) resolutions. Analysis using these velocity fields shows that the production term is systematically negative just prior to the L–H transition, indicating a transfer from mean flows to turbulence, which is inconsistent with the predator–prey paradigm. Moreover, the inferred absolute value of the production term is two orders of magnitude too small to explain the observed rapid L–H transition. These discrepancies are further reinforced by consideration of the ratio between the kinetic energy in the mean flow to the thermal free energy, which is estimated to be much less than 1, suggesting again that the turbulence depletion mechanism may not play an important role in the transition to the H-mode. Although the Reynolds work therefore appears to be too small to directly deplete the turbulent free energy reservoir, order-of-magnitude analysis shows that the Reynolds stress may still make a non-negligible contribution to the observed poloidal flows.

Keywords: confinement, L–H transition dynamics, gas-puff-imaging, zonal flows, Reynolds stress

(Some figures may appear in colour only in the online journal)

1. Introduction

Since the discovery of the high confinement (referred to as the H-mode) regime in the ASDEX tokamak [1, 2], it has become the standard mode of operation of present tokamaks and is planned for future fusion devices such as ITER. This H-mode is associated with the formation of an edge transport barrier that causes a transition from a low (L) to high (H) confinement regime, resulting in improved performance (i.e. temperature, density, and energy confinement time). Operationally, the L–H transition occurs when the injected heat (beam, radio frequency waves, and/or ohmic) exceeds a threshold. The physics governing this transition is, however, unclear, and remains one of the open issues in fusion research.

Most theoretical descriptions of the L–H transition are based on the shear of the radial electric field and coincident $\mathbf{E} \times \mathbf{B}$ poloidal flow shear, which is thought to be responsible for the onset of the anomalous transport suppression [3]. First introduced by Biglari *et al* [4], it is generally supposed that the stabilization of anomalous transport can be achieved by the flow shear via the breaking and/or distortion of edge turbulence eddies. Later, a self-consistent model of the L–H transition was derived from coupled nonlinear envelope equations for the fluctuation level and E_r' [5]. This derived

model is a paradigm that is referred to as the predator–prey model. *The key point of this model is that there is nonlinear energy transfer from turbulence to flows via the Reynolds stress. This transfer drives a sheared zonal* $\mathbf{E}\times\mathbf{B}$ *flow, and concurrently directly depletes the turbulent fluctuations.* Alternatively, the contribution of ∇p_i to E_r can also drive the sheared zonal E × B flows. Depending on the model, turbulence suppression is either due to direct depletion by the Reynolds-stress-induced energy transfer or due to the $\mathbf{E}\times\mathbf{B}$ shearing of eddies, which can in theory reduce the effective growth rate and increase the damping of the turbulent fluctuations. Overall, in the models described above, turbulence suppression is thought to trigger the L–H transition.

Experimentally, several machines (EAST [6], DIII-D [7], C-Mod [8], and HL-2A [9]) have found that turbulence driven mean flows enhance the edge shear flow, which was thought to trigger the L–H transition, essentially consistent with the predator–prey paradigm. However, similar investigations of energy transfer between perpendicular flows and turbulence in the plasma boundary region of the JET tokamak (in ohmic and diverted discharges) have shown that the energy transfer from the zonal flows to turbulence can be both positive and negative in the proximity of sheared flows [10]. Although the latter work was not applied to the L–H transition, it suggests, as an example, that the turbulence can be either pumped or depleted by the sheared flows, pointing to possible ambiguity in using the energy transfer as a key mechanism in the studies.

In this paper, we analyze the L–H transition dynamics on NSTX using the velocimetry of 2D edge turbulence data from gas-puff imaging (GPI). More specifically, we describe turbulence correlation analyses and determine the velocity components at the edge across the L–H transition for 17 discharges with three types of heating power (neutral beam injection—NBI, ohmic, and radio frequency—RF). The turbulence dynamics are examined and the energy transfer between turbulence and mean flow is computed. Using a reduced model equation of edge flows and turbulence, the energy transfer dynamics is compared with the turbulence depletion hypothesis of the predator–prey model of the L–H transition.

2. Underlying model equations

Our analysis will rest on a *minimal model* of edge turbulence and sheared flows, using the very simple two-fluid flux-tube equations of [11], which make the following assumptions: isothermal electrons; a single species of singly-ionized cold ions; purely resistive parallel dynamics; frequencies fast relative to ion transit ($\omega \gg v_{\rm ti}/qR$); and a shearless, simple-circular, large-aspect-ratio magnetic geometry. Although this model must be generalized for detailed quantitative calculations, it is adequate to capture the general structure and make order-of-magnitude predictions. In particular, one may relax any or all of the listed assumptions without changing the qualitative conclusions underlying our data analysis. For example, the same basic conclusions follow from similar analysis of electromagnetic Braginskii equations [12], as well as from radially-global kinetic models that do not separate mean and (arbitrarily large) fluctuations [13].

As shown in [11], our minimal model for edge turbulence nonlinearly conserves a free energy, whose evolution governs the rms amplitude of the turbulent fluctuations. We decompose this free energy into a thermal portion $E_n \doteq \int \mathrm{d}\mathcal{V}\,(T_{\rm e0}/2n_0)n_{\rm e}^2$, a nonzonal $\boldsymbol{E}\times\boldsymbol{B}$ portion $E_\sim \doteq \int \mathrm{d}\mathcal{V}\,\frac{1}{2}n_0 m_i[(\tilde{v}_E^y)^2+(\tilde{v}_E^x)^2]$, and a zonal $\boldsymbol{E}\times\boldsymbol{B}$ portion $E_z \doteq \int \mathrm{d}\mathcal{V}\,\frac{1}{2}n_0 m_i\langle v_E^y\rangle^2$, with x and y the radial and binormal coordinates, $v_E^x \doteq \boldsymbol{v}_E\cdot\nabla x$ and $v_E^y \doteq \boldsymbol{v}_E\cdot\nabla y$ components of the $\boldsymbol{E}\times\boldsymbol{B}$ drift, $\int \mathrm{d}\mathcal{V}$ a volume integral, $\langle\cdots\rangle$ the flux surface average, and tildes indicating the nonzonal portion, e.g. $\tilde{v}_E^y \doteq v_E^y - \langle v_E^y\rangle$. The energy balance reads:

$$\partial_t E_n = T_{\rm e0}\int \mathrm{d}\mathcal{V}\left[n_{\rm e}v_E^x\frac{1}{L_n} - \phi\mathcal{K}(n_{\rm e}) - \frac{1}{n_0 e}j_\parallel\nabla_\parallel n_{\rm e}\right], \quad (1)$$

$$\partial_t E_\sim = \int \mathrm{d}\mathcal{V}\,[T_{\rm e0}\tilde{\phi}\mathcal{K}(n_{\rm e}) + j_\parallel\nabla_\parallel\phi - n_0 m_i(\tilde{v}_E^x\tilde{v}_E^y)\partial_x\langle v_E^y\rangle], \quad (2)$$

$$\partial_t E_z = \int \mathrm{d}\mathcal{V}\,[T_{\rm e0}\langle\phi\rangle\mathcal{K}(n_{\rm e}) + n_0 m_i(\tilde{v}_E^x\tilde{v}_E^y)\partial_x\langle v_E^y\rangle], \quad (3)$$

in which the curvature operator is defined as $\mathcal{K} \doteq -(2/B^2)\hat{\boldsymbol{b}}\times\nabla B\cdot\nabla$ and $\mathcal{K}^x \doteq -(2/B^2)\hat{\boldsymbol{b}}\times\nabla B\cdot\nabla x$. Note that in equations (1)–(3), we have discarded boundary terms. These terms are typically somewhat small, but may become comparable in magnitude to the corresponding retained terms if turbulent or zonal flow wavelengths approach the radial width of the domain.

In experimental investigations of energy balance across the L–H transition, it is important to retain equation (1), as was done in the original predator–prey model [5], along with equations (2) and (3), for the following reason [11]: the parallel current $j_\parallel$ mediates an energy transfer between $E_{\tilde{n}}$ and $E_\sim$ on rapid electron transit timescales, acting until electrons approach adiabatic response, which corresponds to an energy ratio

$$\frac{E_\sim}{E_{\tilde{n}}} = \frac{\int \mathrm{d}\mathcal{V}\,\tilde{v}_E^2/c_s^2}{\int \mathrm{d}\mathcal{V}\,\tilde{n}_{\rm e}^2/n_0^2} \sim k_\perp^2\rho_s^2, \quad (4)$$

for $\tilde{v}_E^2 = (\tilde{v}_E^x)^2+(\tilde{v}_E^y)^2$, $k_\perp$ a typical perpendicular wave number of the turbulence, and ρ_s and c_s the ion gyroradius and sound speed evaluated at the electron temperature. Since the Reynolds work $n_0 m_i(\tilde{v}_E^x\tilde{v}_E^y)\partial_x\langle v_E^y\rangle$ typically causes energy evolution on timescales much longer than electron transit, an ordering that holds for our observations, it cannot strongly change the ratio $E_\sim/E_{\tilde{n}}$.[3] So, in order to directly suppress the turbulence, it must deplete the total turbulent energy $(E_{\tilde{n}}+E_\sim)$, which is approximately equal to $E_{\tilde{n}}$ for the typical edge turbulence case $k_\perp\rho_s \sim 0.1$. On timescales faster than poloidal rotation damping, this requires

[3] To roughly estimate the parallel electron response time at perpendicular length scales rather larger than ρ_s, choose the slowest of the following three rates: collisional parallel electron diffusion $\sim k_\parallel^2 v_{te}^2/k_\perp^2\rho_s^2\nu_{ei}$, free/collisionless parallel electron flow $\sim k_\parallel v_{te}/k_\perp\rho_s$, or shear Alfven/electromagnetic $\sim k_\parallel v_A$. For our parameters, these rates are about $5.5\cdot10^7\ \mathrm{s}^{-1}$, $4.8\cdot10^6\ \mathrm{s}^{-1}$, and $2.6\cdot10^5\ \mathrm{s}^{-1}$, respectively—all much more rapid than the L–H transition.

$$\frac{E_z}{E_{\tilde{n}}} = \frac{\int \mathrm{d}\mathcal{V}\,\langle v_E^y\rangle^2/c_s^2}{\int \mathrm{d}\mathcal{V}\,\tilde{n}_e^2/n_0^2}, \quad (5)$$

to be order unity, with $E_{\tilde{n}}$ evaluated immediately pre-transition and using the increase in E_z over the transition.[4,5]

To determine the evolution of the flow shear, we may use the zonal vorticity equation

$$n_0 m_i \partial_t \partial_x \langle v_E^y \rangle = -n_0 m_i \partial_x^2 \langle \tilde{v}_E^x \tilde{v}_E^y \rangle - T_{e0} B \partial_x \langle \mathcal{K}^x n_e \rangle, \quad (6)$$

showing that up to a spatially constant (but possibly time-dependent) offset, the poloidal rotation evolves in response to the Reynolds stress divergence (i.e. $\partial_x \langle \tilde{v}_E^x \tilde{v}_E^y \rangle$), along with a curvature term that mediates poloidal rotation damping. Since poloidal rotation is typically damped towards its neoclassical value at a rate of order of the ion transit frequency $\nu \sim v_{ti}/qR$ [14, 15], the Reynolds stress contribution to the poloidal rotation may be very crudely estimated from equation (6) as $\langle v_E^y \rangle \sim -\nu^{-1} \partial_x \langle \tilde{v}_E^x \tilde{v}_E^y \rangle \sim -(qR/v_{ti}) \partial_x \langle \tilde{v}_E^x \tilde{v}_E^y \rangle$. Although this estimate is too rough for detailed quantitative comparison, it is adequate for an order-of-magnitude check.

In principle, the flux surface average is a poloidal and toroidal average over an entire flux surface. However, since the GPI diagnostic only views a small fraction of the surface (see section 3 below for details), the poloidal spatial average over the GPI view is a poor approximation of the total flux-surface average. For this reason, we estimate the flux-surface average of velocity with a combination of a poloidal average (across the field of view) and a low-pass frequency filter (here, a cutoff at 1 kHz was used), exploiting a typical separation in frequency scales between the slow temporal evolution of the zonal component and the fast temporal evolution of the turbulent fluctuations.

3. Experimental approach

Since GPI is central to the analysis described here, we provide a brief description of the GPI system on NSTX. We refer the reader to a more extensive description of the GPI diagnostics elsewhere [16, 17]. GPI diagnostics are used to image the turbulent fluctuations in the edge of fusion devices. This diagnostic in NSTX relies on a deuterium gas puff into the plasma via a gas manifold. The visible neutral line emission of D_α at 656 nm from the cloud is then imaged using a fast framing camera. The camera views are aligned with a magnetic field pitch angle of ~36 degrees, which enables optimum spatial resolution in the radial versus binormal plane, where the binormal direction is perpendicular to the magnetic field within the flux surface. The GPI field of view is centered 20 cm above the outer midplane spanning the separatrix. This view spans a region of 24 cm by 30 cm (radial and poloidal directions) with a spatial resolution of ~1 cm at 400 kHz sampling rate. The directions x, y labeled in the above section correspond, respectively, to radial r and poloidal θ in the remainder of the text. For the study presented below, the collected images are normalized by time-averaged images and then analyzed for the spatial correlations (radial and poloidal lengths). Furthermore, these images are processed using velocimetry techniques to determine the velocity fields and to compute the various terms in the model equations highlighted in section 2 in order to test the L–H models.

3.1. Turbulence characteristics

Edge turbulence characteristics across the L–H transitions in NSTX were described previously using GPI data taken in 2009 [18], and the present database from 2010 shows the same general characteristics. The most dramatic change at the L–H transition is a rapid reduction in relative GPI light fluctuation levels ($\tilde{I}/\bar{I}$) inside and near the separatrix ($\tilde{I}$ are the rms fluctuations and $\bar{I}$ are the mean intensity fluctuations of the GPI signal), which occur within ~100 μs of the L–H transition time as seen in the standard D_α diagnostics.

Examples of the radial profiles of the GPI signal level and its relative fluctuation level just before and after the L–H transition are shown in figure 1. It is clear from figure 1(*a*) that the average GPI radial profile shifts inward in the H-mode phase. In this phase, the fluctuation levels drop inside the separatrix relative to the L-mode phase. Furthermore, figure 1(*b*) indicates that the maximum level of fluctuations in the L-mode occurs approximately 1 cm inside the separatrix.

Figure 2(*a*) shows the time dependence of the relative GPI fluctuation level averaged over all 17 shots in the present database (see table 1) located 1 cm inside the separatrix. These times are measured with respect to the time at which the GPI fluctuation level transitions to the H-mode state in each shot, which has an uncertainty of about ±0.1 ms. There is no significant time variation in the relative fluctuation level during the ~3 ms preceding the transition, and the sudden drop at the transition from $(\tilde{I}/\bar{I}) \sim 25\%$ to ~15% occurs consistently over ~0.1 ms. Note that the shot-to-shot variations during the L-mode period, in figure 2(*a*), are ~4% in $\tilde{I}/\bar{I}$.

Figures 2(*b*) and (*c*) display the time history of the radial (L_{rad}) and poloidal (L_{pol}) lengths (FWHM) across the L–H transition 1 cm inside the separatrix. There is no significant change in the average poloidal or radial correlation lengths during the ~3 ms preceding the transition. However, there is a significant increase in the average poloidal correlation length, and a decrease in the average radial correlation length over the ~1 ms period after the transition. The shot-to-shot

[4] Resistive dissipation implies that the transfer of energy from E_n to $E_\sim$ is at least somewhat lossy. However, even in a strongly nonadiabatic case where $\tilde{h}_e \doteq \tilde{n}_e/n_0 - e\tilde{\phi}/T_{e0}$ is comparable in magnitude with $e\tilde{\phi}/T_{e0}$, the resistive dissipation $\eta j_\parallel^2 = j_\parallel \nabla_\parallel (T_{e0}\tilde{h}_e/e)$ is only of comparable size with the energy transfer into $E_\sim$ [$j_\parallel \nabla_\parallel \tilde{\phi}$]. So, even in that case, the predator–prey model requires $E_z/E_{\tilde{n}} \sim 1/2 \sim O(1)$.

[5] On slow enough timescales, equation (5) is modified by poloidal rotation damping. Modeling the curvature term in equation (3) as $-\nu E_z$ for a poloidal rotation damping rate ν around v_{ti}/qR, we can time-integrate the energy balance over the L–H transition

$$-\Delta|_{R.S.}(E_n + E_\sim) = \int \mathrm{d}t \int \mathrm{d}\mathcal{V}\, n_0 m_i (\tilde{v}_E^x \tilde{v}_E^y) \partial_x \langle v_E^y \rangle = \Delta E_z + \int \mathrm{d}t\ \nu E_z,$$

where Δ indicates the H-mode value minus the L-mode value, and subscript R.S. means 'due to Reynolds stress.' To roughly estimate the effect of Reynolds stress, we may take $\int \mathrm{d}t\ \nu E_z \to (\nu\tau_{L-H})E_z$. In our data, $(\nu\tau_{L-H}) \lesssim 1$, so poloidal flow damping may relax equation (5) only by roughly a factor of 2.

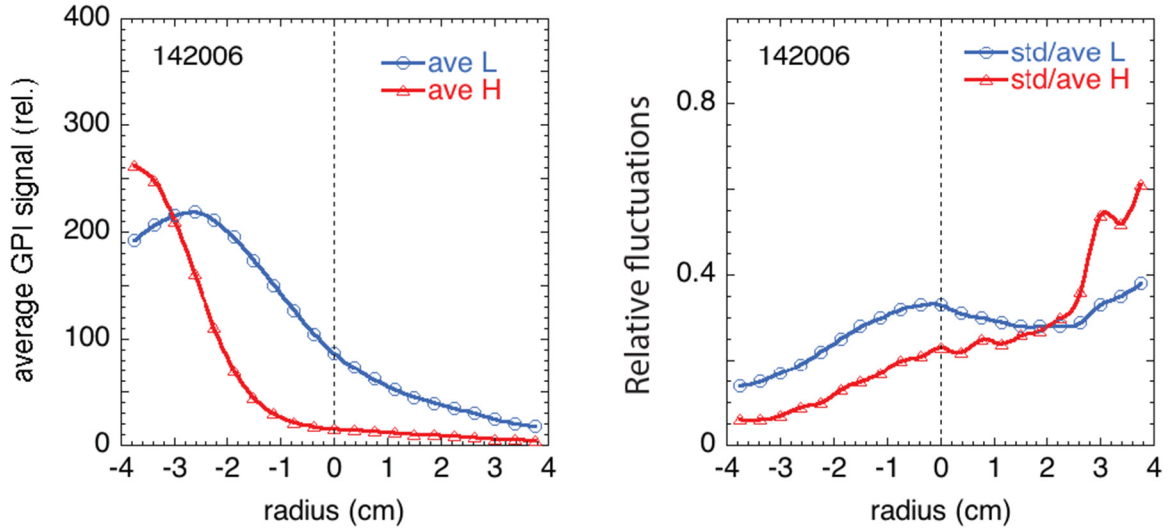

Figure 1. Radial profiles of the GPI signal (left panel) and its relative fluctuation level (right panel), averaged over the L and H-mode periods for the RF discharge 142 006. The radial profiles change in response to rapid electron density and temperature changes at the transition. The relative fluctuation level decreases by about a factor-of-two inside and near the separatrix. The dashed line represents the separatrix.

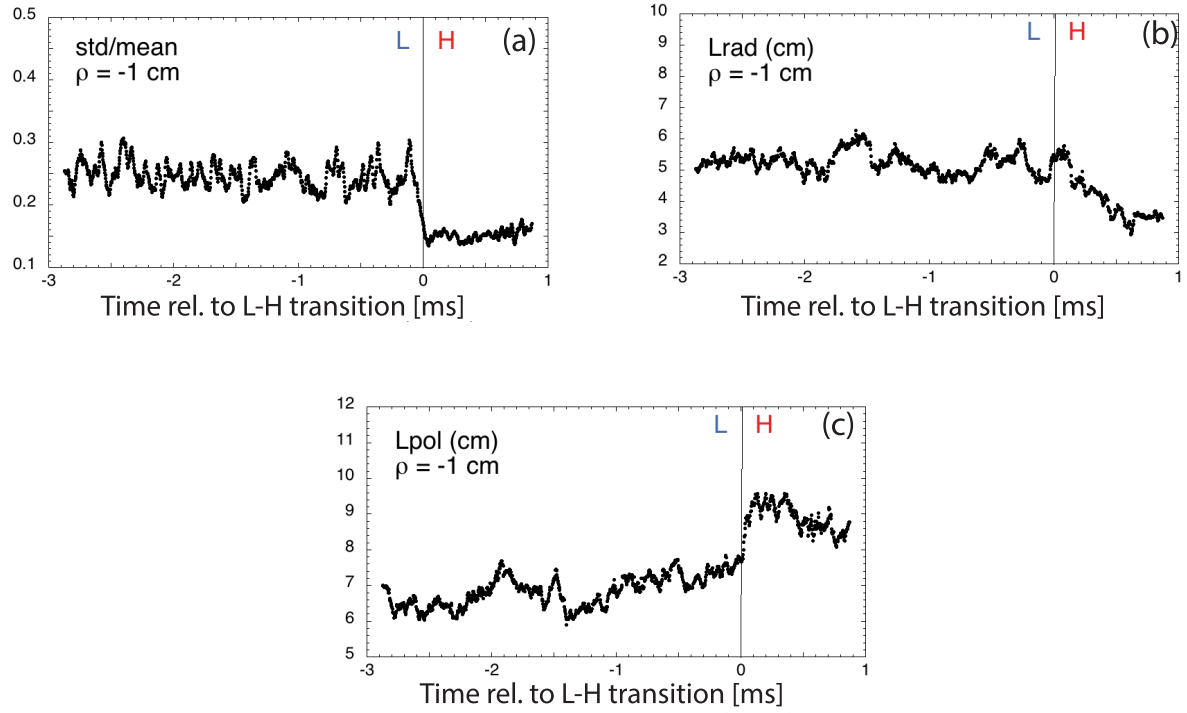

Figure 2. (*a*) Relative fluctuation levels for multiple discharges across the L–H transition: the averaged relative fluctuation levels show, for all discharges, a reduction in the fluctuation level across the L–H transition. (*b*) The average radial correlation length decreases after the H-mode transition, and (*c*) the average poloidal correlation length increases after the transition, averaged over all the discharges at 1 cm inside the separatrix. There are no significant changes in these correlation lengths before the transition.

variations during the L-mode period are ±1.0 cm in the poloidal correlation length and ±1.2 cm in the radial correlation length.

The poloidal and radial turbulence velocities were also evaluated using the same time-delayed cross-correlation technique as in [18]. These velocities were evaluated at each radius versus time by averaging over ±30 μs, then averaging over 22 cm poloidally within the GPI image. The results at 1 cm inside the separatrix are shown for all the shots from table 1 in figure 3, along with the shot averages in black. There was a considerable spread in velocities from shot-to-shot, but the shot-averaged velocities did not vary significantly versus time during the 3 ms before the L–H transitions (at least above about ±1 km s^{-1}). Across the L–H transition there seems to be an increase in the shot-averaged poloidal velocity from −0.8 km s^{-1} to +0.4 km s^{-1} (toward the electron diamagnetic drift direction), and a slight decrease in the shot-averaged radially outward velocity from 0.7 km s^{-1} to 0.6 km s^{-1}. Overall,

Table 1. Database of L–H transition discharges. The color code indicates the different heating schemes during the L–H transition.

Shot	L-H time [ms]	Btor [kG]	Plasma current [kA]	NBI Power [MW]	RF Power [MW]	Heating Schemes
138113	254.9	4.4	910	1.4	-	NBI
138114	252.5	4.4	910	1.4	-	NBI
138115	243.0	4.4	910	0	-	NBI
138116	251.6	4.4	910	0	-	NBI
138117	245.8	4.4	910	0	-	NBI
138118	249.5	4.4	910	0	-	NBI
138119	268.4	4.4	910	1.2	-	NBI
139955	364.3	4.4	900	1.0	-	NBI
142229	401.8	4.4	800	1.0	-	NBI
141745	227.7	3.6	800	-	-	Ohmic
141746	244.9	3.6	800	-	-	Ohmic
141747	226.5	3.6	800	-	-	Ohmic
141751	235.0	3.6	800	-	-	Ohmic
141919	231.1	4.4	910	-	0.64	RF
141920	241.5	4.4	910	-	0.60	RF
141922	237.5	4.4	910	-	0.73	RF
142006	223.0	4.4	910	-	0.5	RF

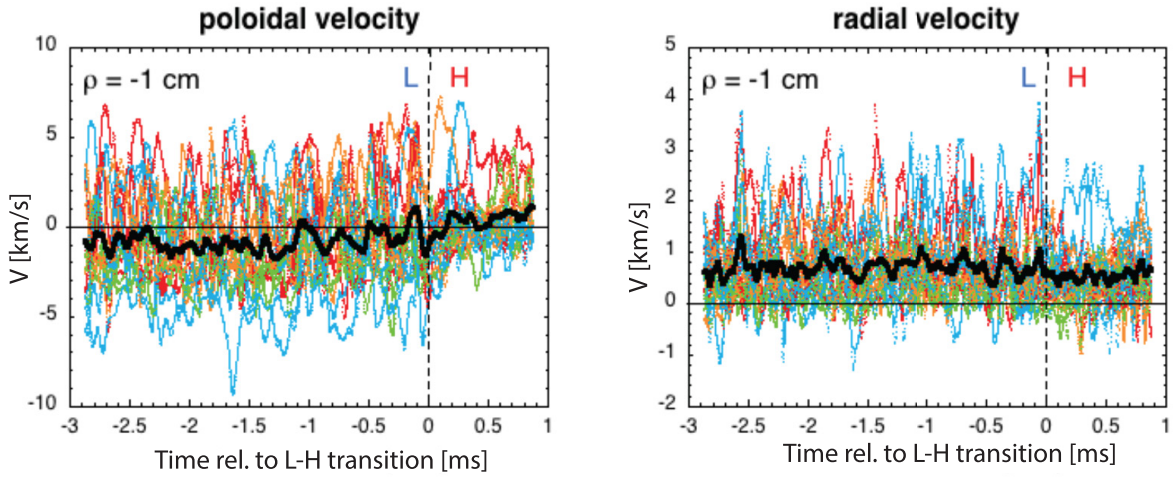

Figure 3. Time dependence of the poloidal and radial velocities for all 17 shots in the database (colored lines), and their averages (black lines), all evaluated 1 cm inside the separtrix. These velocities are calculated from time-delayed cross-correlation functions averaged over 30 μs and 22 cm in the poloidal direction. There is no significant change in the shot-averaged velocities during the 3 ms preceding the L–H transition, but there are slight changes from before to after the transition.

within the error bars, there is no clear observation of an L–H transition trigger.

Some of the variation in the poloidal velocity for the individual shots in figure 3 prior to the L–H transition is due to a poloidally oscillating 'zonal flow' described earlier for GPI in NSTX [18, 19]. An example of these poloidal flow oscillations for one shot is shown in figure 4, in which the time evolution of the poloidal velocity is plotted in color versus the radial and poloidal coordinates. Such zonal flows in NSTX can extend across most of the poloidal range of the GPI view, and over the radial range near and inside the separatrix. As seen previously [18, 19], these oscillations are found in the frequency range ~2–5 kHz during the 30 ms preceding the L–H transition for most (but not all) of the shots in table 1. However, there is no systematic increase in the amplitude of these flows just prior to the L–H transition, and in some cases similar flows also exist after the L–H transition. Further analysis of these flows is interesting but beyond the scope of the present paper.

3.2. Application of velocimetry to GPI

To evaluate the energy exchange dynamics using GPI, we use high resolution velocimetry to measure the local 2D turbulence motion, and assume that the turbulence motion is equivalent to the local $\mathbf{E} \times \mathbf{B}$ fluid motion. This is a common assumption in the analysis of GPI [8], beam-emission-spectroscopy (BES) [20], and Doppler reflectometry diagnostics of

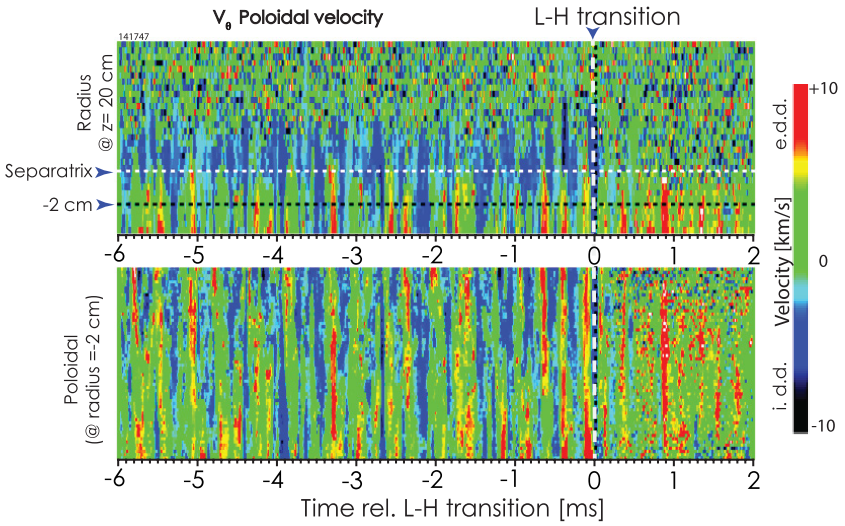

Figure 4. Calculated radial and poloidal profiles of the poloidal velocity versus time for one shot (141747) based on time-delayed cross-correlation analysis. The magnitude of the poloidal velocity is shown by the color bar at the upper right. There is a poloidal flow oscillation in the radial region near and inside the separatrix (top panel), which often extends 22 cm across the poloidal range of the GPI view (bottom panel), over a time period at least 6 ms before the transition. The radial profile is evaluated near the vertical center of the GPI view, and the poloidal profile is evaluated 2 cm inside the separatrix for this case.

edge turbulence [21], but is only approximately true due to polarization effects at small scales and possible contributions of the parallel electron heat flux. There are also systematic limitations and uncertainties in any velocimetry analysis of GPI data, such as the well-known 'barber-pole' effect, as discussed in [22, 23]. Both of these uncertainties are special cases of a more general limitation, namely that velocimetry techniques only see velocities parallel to the intensity gradient. Therefore, velocities along exact isocontours of intensity are invisible, although small intensity fluctuations can be tracked successfully given a sufficient signal/noise level. This is an unavoidable ambiguity that is shared by GPI velocimetry, BES velocimetry, and any other analogous techniques. Such ambiguity is particularly evident in the H-mode phase where the images sometimes have very low fluctuation levels.

To extract the time varying 2D velocity field $\mathbf{v}(r,\theta,t)$ from the intensity fluctuations recorded with the GPI diagnostic, we use the orthogonal dynamic programming (ODP) technique. The ODP technique is described in detail in [24] and the salient features are only discussed briefly here. ODP is a robust technique for searching optical alignments of patterns through the simple realization of cross correlation. The procedure is essentially the search of a transformation that relates the consecutive image with the previous image in a time series, and minimizes the Minkowski distance $L_n = \sum_i \sum_j |I_0(i,j) - I_1(i,j)|^n$ between them. The key feature of the algorithm is to reduce the problem of determining 2D displacements into a series of 1D displacements selected carefully to reduce the complexity of the task. Each image of the temporally separated pair is sliced into several parallel overlapping strips (here along the r direction), as shown in figure 1 of [24]. The velocity is estimated from the distortion or transformation, in the slicing direction, necessary to minimize the calculated intensity difference. The whole process is iterated several times to achieve higher spatial resolution similar to the actual pixel resolution of the image. The width of the strips and the corresponding overlaps are reduced by about $\sqrt{2}$ in each radial–poloidal (r-θ) iteration.

This technique has the merit of determining the velocity field at the sampling time and with spatial resolution close to that of the images, both of which are advantages over the commonly used time-delay estimate (TDE) velocity reconstruction (i.e., figure 3). It is worth noting that ODP showed overall good agreement (∼80% correlations) when compared with the commonly used TDE velocity reconstruction, which has a much longer (∼30 μs) time resolution. Similarly, ODP was also compared with the spatial Fourier harmonics approach (to be described elsewhere) and showed ∼80% correlation. For the remainder of the paper, only the velocimetry using the ODP will be discussed. Displayed in figure 5 is an example of the ODP 2D reconstructions of the velocity data.

Previous probe measurements of the energy transfer [6, 9] faced several challenges, mainly due to the spatial undersampling of the region of interest. GPI offers more spatial points than probes do, reducing this challenge. Here, we compute the Reynolds stress ($\langle\tilde{v}_\theta\tilde{v}_r\rangle$) and the production term ($\langle\tilde{v}_\theta\tilde{v}_r\rangle\partial_r\langle\bar{v}_\theta\rangle$) to qualitatively provide the energy transfer direction during L–H transition. All operations are defined in the next section. The key metric is the energy transfer between mean flows to turbulence, which is directly related to the momentum flux and the radial gradient in the mean flow (i.e. the production term). This quantity can be either positive (from turbulence to driven flows) or negative (from DC (zonal) flows to turbulence).

3.3. Energy transfer computations: results

We have computed the 2D velocity data $\mathbf{v} = \bar{\mathbf{v}} + \tilde{\mathbf{v}}$, $\forall(r,\theta,t)$, where r represents the radius, θ describes the poloidal direction, and t is the time. Figures 6–8 show the flow velocities and derived parameters, namely, the poloidally averaged poloidal flow, its shear, the Reynolds stress, and the production term,

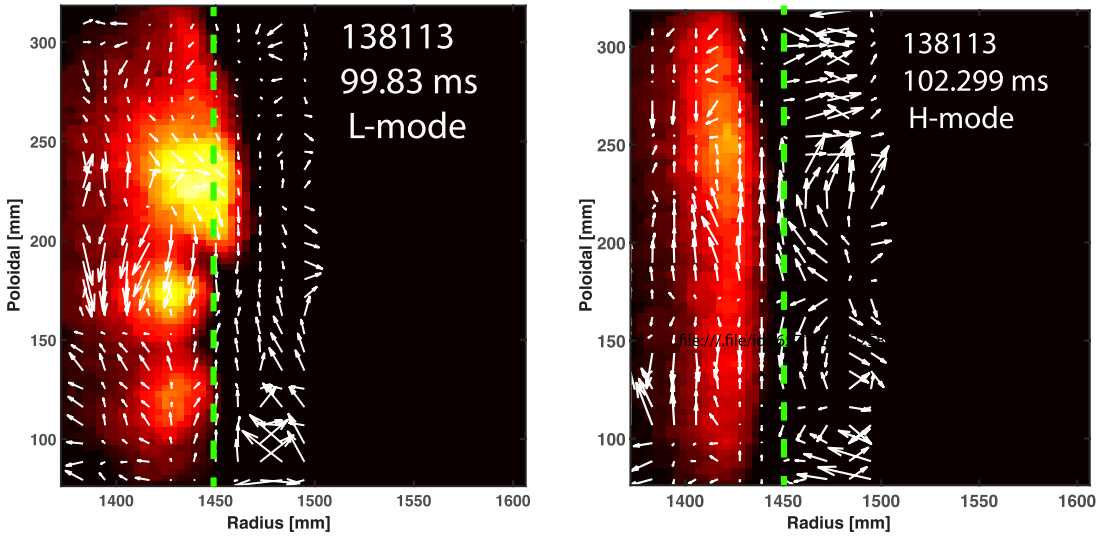

Figure 5. Examples of the GPI intensity images where the arrows represent the velocity vectors. The vertical green dotted line indicates the separatrix location (with ±1 cm uncertainty).

for three types of heating schemes. For these figures, all these quantities are computed at a radial position 1 cm inside the last closed flux surface, which, in addition to being where the maximum fluctuation level of fluctuations occur (see figure 1(*b*)), is typically the center of the 2–3 cm wide pedestal gradient region most relevant for the study of the L–H transition in NSTX (see figure 6 in [25]). The shaded area in each panel around each solid line represents the standard deviations for all discharges of the same heating scheme. For instance, in the NBI case, we only choose the discharges in table 1 with NBI heating and average over them. The horizontal axis represents the time relative to the L–H transition where '$t = 0$' indicates the L–H transition determined with 100 μs uncertainty. A 1 kHz cutoff was applied to the raw velocity profiles to separate the mean flow from the fluctuating flow. More specifically, the mean flow ($\tilde{\mathbf{v}}$) is given by low-pass filtering the raw velocity at 1 kHz and the fluctuating component of the flow ($\tilde{\mathbf{v}}$) is given by high-pass filtering the raw velocity. This cutoff frequency was chosen to include the poloidally oscillating flow (2–5 kHz) described in [18, 19] into the non zonal component. Such an approach was also used in the analysis of [8]. Note that choosing an alternate cutoff frequency that includes the poloidal oscillation in the zonal component does not qualitatively change the results presented in this paper. The angular brackets ($\langle ... \rangle$) define the poloidal-average over the 22 cm (GPI view) instead of the flux surface average (see the end of section 2 where a justification is provided).

In the RF and ohmic cases, the total poloidal flow averaged poloidally (figures 7(*a*) and 8(*a*)) becomes positive (i.e. in the electron diamagnetic drift direction) after the L–H transition. The NBI case (figure 6(*a*)) shows no *significant* change before and after the L–H transition. In all three types of heating schemes, the magnitude of the shear in the mean poloidal velocity *decreases* after the L–H transition (panels (b) of figures 6–8). Note that it is the absolute value of the shear that is responsible for shearing apart the eddies. For all heating schemes, this decreasing absolute value of the shear across the L–H transition is inconsistent with the idea that flow shear is suppressing the turbulence, as described in [4]. However, GPI emission bands become radially narrow across the L–H transition and the fluctuation level drops in the H-mode. So it is possible that the decrease in our inferred flow shear in the H-mode might be a result of the low fluctuation level, and consequent difficulty in evaluating velocity in our analysis.

Below, we now show three different approaches for testing the energy exchange dynamics across the L–H transition. First, we look at the exchange dynamics using the Reynolds stress and production term. Panels (*c*) and (*d*) of figures 6–8 display the Reynolds stress and production term across the L–H transition 1 cm inside the separatrix. In these figures, the Reynolds stress and production term clearly decrease to a mean value of zero in the H-mode. In addition, the rms fluctuations of the Reynolds stress, as well as that of the production term, are significantly reduced in the H-mode phase compared to the L-mode phase. Unlike the results of [8], there is no systematic peaking of the Reynolds stress, except in the NBI case (figure 6(*b*)) prior to the L–H transition, which shows an increase by about one standard deviation.

Further, contrary to expectations of the predator–prey model's predictions, we systematically observe a negative production term just prior to the L–H transition 1 cm inside the separatrix, suggesting a transfer of energy from mean flows to turbulence. Despite this implication that shear flows are apparently exciting the turbulence, figure 2 shows that the turbulence levels drop across the L–H transition. These observations can only be reconciled if a different term in the energy balance equations becomes strongly negative at the L–H transition, overwhelming the Reynolds work to cause turbulence suppression.

Second, to address the above point, we recall from section 2 and [11] that for the energy transfer to mean flows to contribute significantly to the depletion of the turbulence, the condition $\frac{\langle \tilde{v}_\theta \rangle^2 / c_s^2}{(\tilde{n}_e / n_{e0})^2} \gtrsim 1$ is required. Note that $(\tilde{n}_e/n_{e0})^2$ is that of the L-mode phase so that the ratio to be compared becomes $\eta \doteq \frac{\langle \tilde{v}_\theta \rangle^2 / c_s^2}{(\langle \tilde{I}^2 \rangle_{[L]} / \bar{I}^2)}$, where $(\tilde{n}_e/n_{e0}) \sim \tilde{I}/\bar{I}$, and $\langle \tilde{I}^2 \rangle_{[L]}^{1/2}$ is the rms of the GPI intensity fluctuations over the L-mode phase

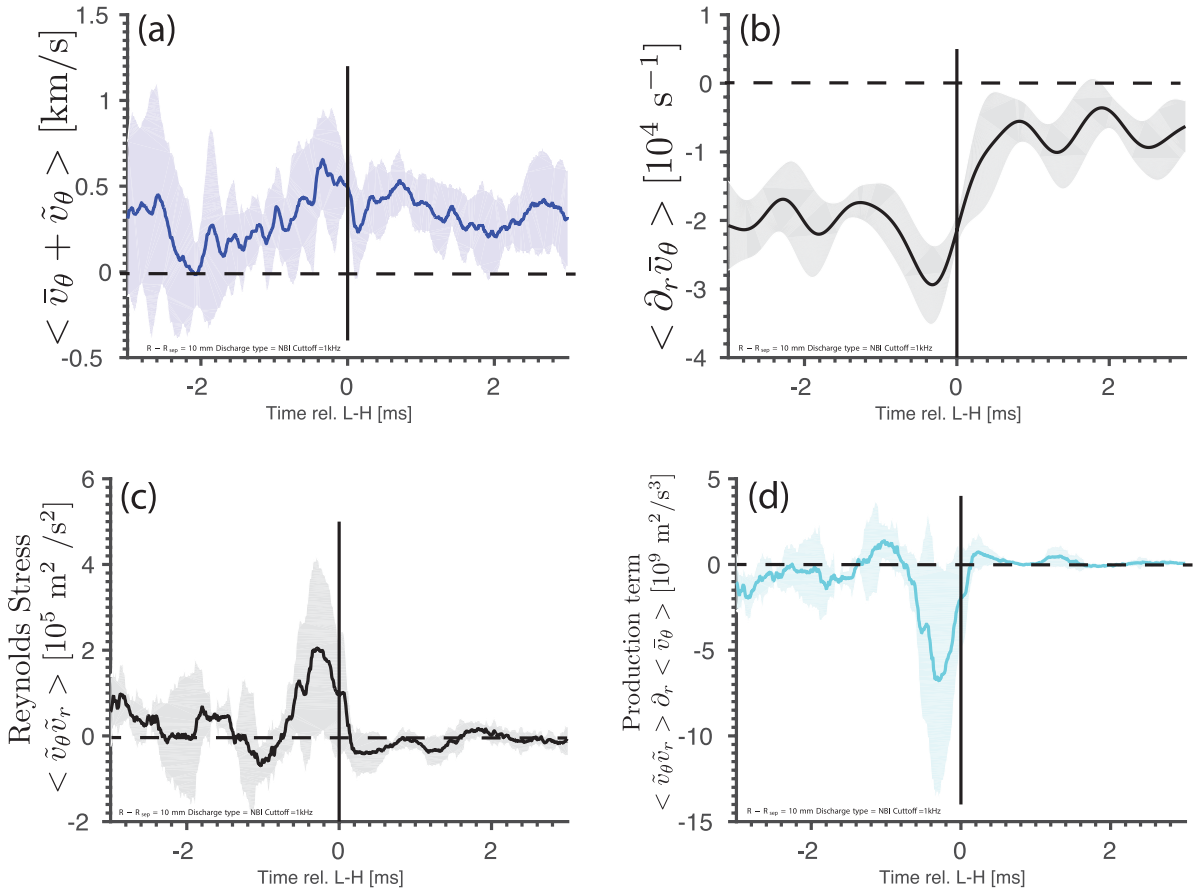

Figure 6. NBI case: flows and derived quantities across the L–H transition 1 cm inside the separatrix. (*a*) Poloidal flow velocity containing both mean and fluctuating component $\langle \bar{v}_\theta + \tilde{v}_\theta \rangle$. (*b*) The shear in the mean poloidal flow $\langle \bar{v}_\theta \rangle$ appears to increase across the L–H transition. (*c*) The Reynolds stress $\langle \tilde{v}_\theta \tilde{v}_r \rangle$ peaks prior to the L–H transition. (*d*) The production term $\langle \tilde{v}_\theta \tilde{v}_r \rangle \partial_r \langle \bar{v}_\theta \rangle$ is negative during the L–H transition. The shaded area represents the standard deviation from all the NBI discharges.

at a given radius. Figures 9(*a*), 10(*a*), and 11(*a*) display the time-dependent radial profiles of this energy ratio for the three types of heating schemes across the L–H transition. These figures show that the kinetic energy in the mean flow (proportional to $\langle \bar{v}_\theta \rangle^2 / c_s^2$) remains much smaller than the thermal free energy (proportional to $(\tilde{n}_e/n_{e0})^2$) at all radii with clear GPI signals. Note that the radial structure of the energy ratio in the L-mode phase is shifted inward during the H-mode phase. The two order magnitude difference (see figures 9–11) in the energies substantiates the argument that the energy associated with the mean flow is unable to account for the depletion of the turbulence energy, even allowing for some order-unity inaccuracy due to resistivity, poloidal flow damping, and approximations made in the theoretical model. As stated above, the depletion is the fundamental aspect of the predator–prey model, resulting in a discrepancy with our data. In other words, the energy transfer due to Reynolds stress appears much too small to directly deplete the energy in the turbulence.

Third, we examine how long the L–H transition would take given this production term. We refer to this production generated L–H transition time as τ^{RS}_{L-H}. We estimate this by taking the ratio $\tau^{RS}_{L-H} = E_{\tilde{n}}/(n_0 m_i \langle \tilde{v}_\theta \tilde{v}_r \rangle \partial_r \langle \bar{v}_\theta \rangle) \Leftrightarrow \tau^{RS}_{L-H} = 0.5 c_s^2 (\tilde{n}_e/n_{e0})^2 / (\langle \tilde{v}_\theta \tilde{v}_r \rangle \partial_r \langle \bar{v}_\theta \rangle)$, where $E_{\tilde{n}} \doteq (n_0 T_{e0}/2)(\tilde{n}/n_0)^2$. Assuming typical separatrix electron temperature $T_e \sim 60$ eV, $(\tilde{n}_e/n_{e0}) \sim 0.25$ (see figure 2(*a*) just prior to the L–H transition), and the production term given by panels (d) of figures 6–8 of about $5 \cdot 10^9$ m^{-2} s^{-3}, we get a dimensional time indicating that the L–H transition duration τ^{RS}_{L-H} should be about 18 ms, which is far too long compared to the observed time of $\tau^{exp}_{L-H} \sim 100$ μs based on the fluctuation drop. This suggests that a much larger production term would be necessary to explain the typical L–H transition times.

Another way to look at this is to compare the production term (P) to the change in the thermal free energy (P_0) between the L and H mode phases. For the production term to be large enough to deplete the turbulence energy, the ratio $\frac{P}{P_0} \doteq \frac{n_0 m_i (\tilde{v}_E^x \tilde{v}_E^y) \partial_x \langle v_E^y \rangle}{(\tau^{exp}_{L-H})^{-1} (E_{\tilde{n}}|_L - E_{\tilde{n}}|_H)}$ should be order unity. Here τ^{exp}_{L-H} is the L–H duration time (approximately 100 μs), and $n_0 m_i (\tilde{v}_E^x \tilde{v}_E^y) \partial_x \langle v_E^y \rangle$ is the production term. $E_{\tilde{n}}|_L$ and $E_{\tilde{n}}|_H$ represent the thermal free energy averaged in the L and H phases, respectively. Here, $(\tilde{n}/n_0)^2$ is approximated by $(\tilde{I}_{gpi}/\bar{I}_{gpi})^2$. An example of such a ratio is given in figure 12 for the ohmic case 1 cm inside the separatrix (the RF and NBI cases are not shown here—both give similar less than unity ratios). This figure shows that this ratio is always two orders of magnitude less than 1, demonstrating again that the turbulence depletion

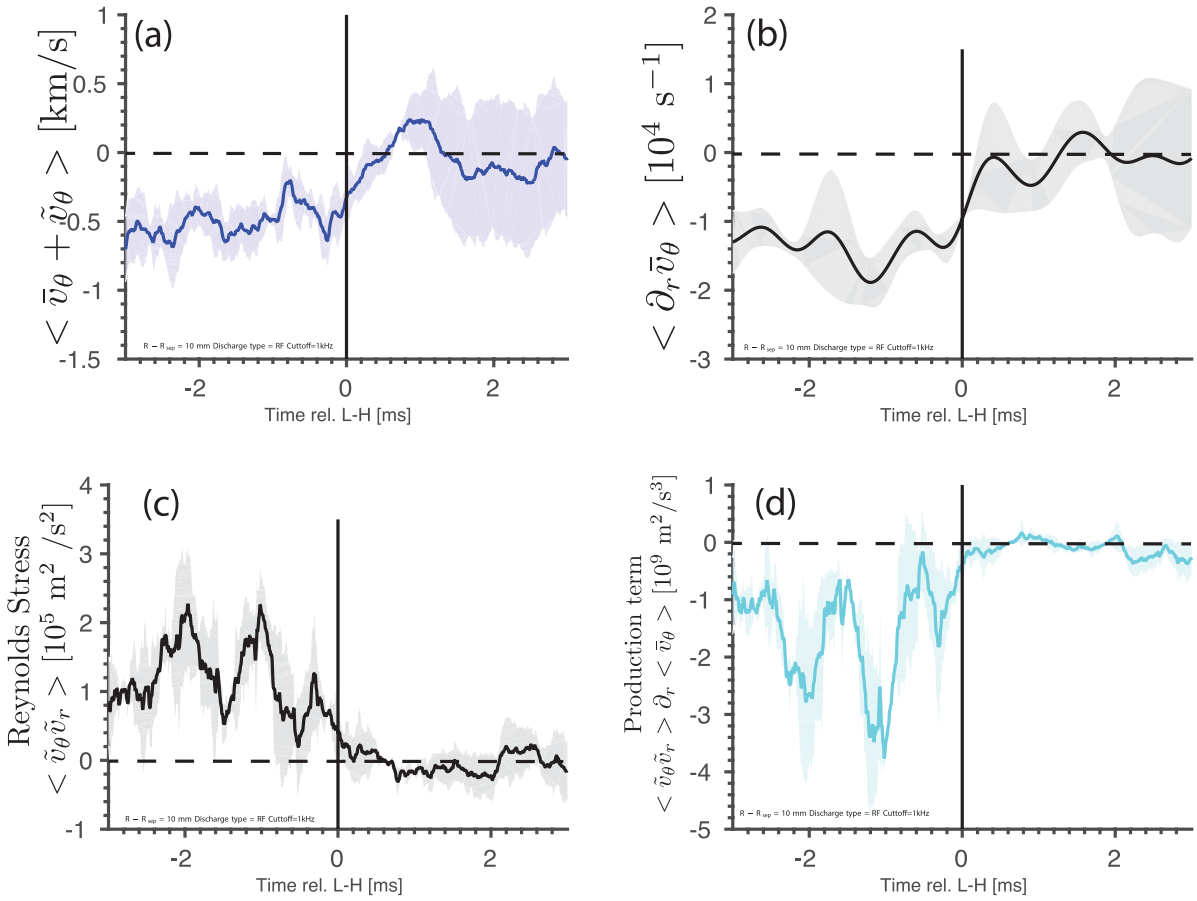

Figure 7. RF case: flows and derived quantities across the L–H transition 1 cm inside the separatrix. See figure 6 for captions.

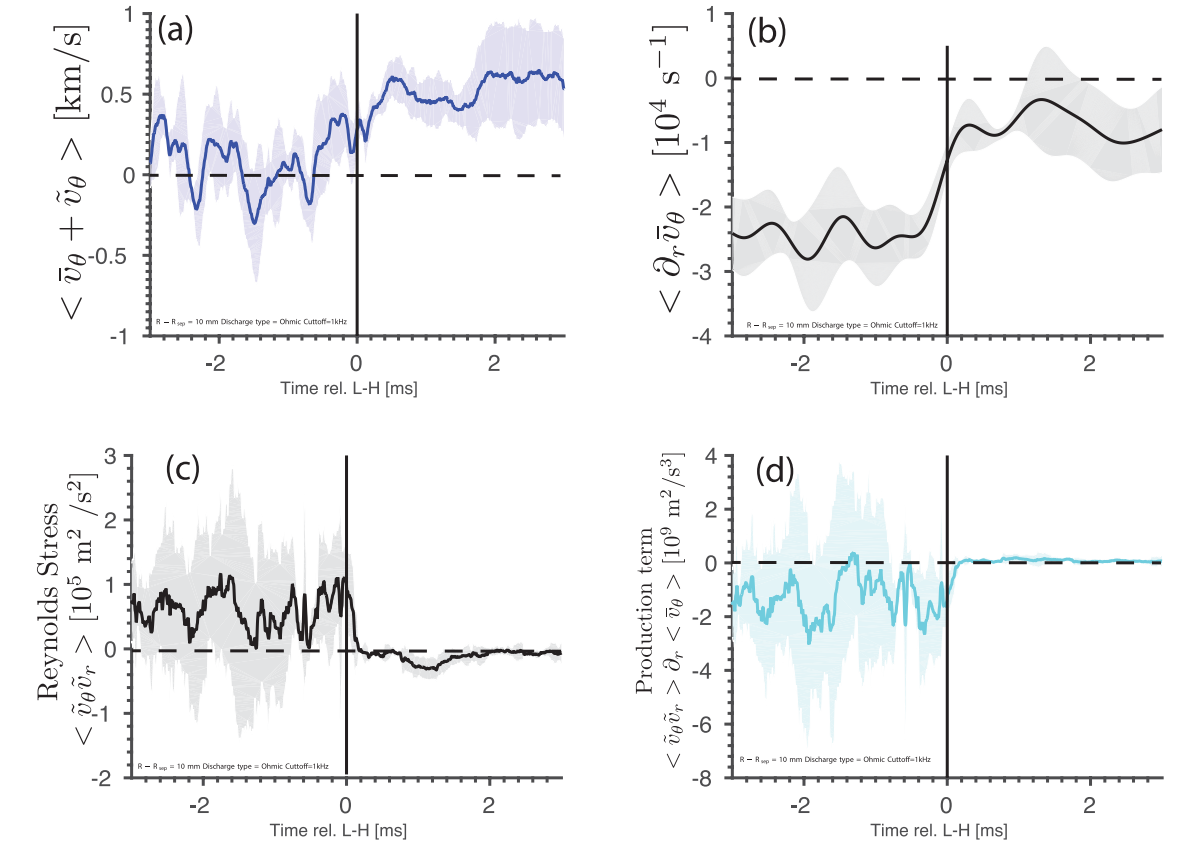

Figure 8. Ohmic case: flows and derived quantities across the L–H transition 1 cm inside the separatrix. See figure 6 for captions.

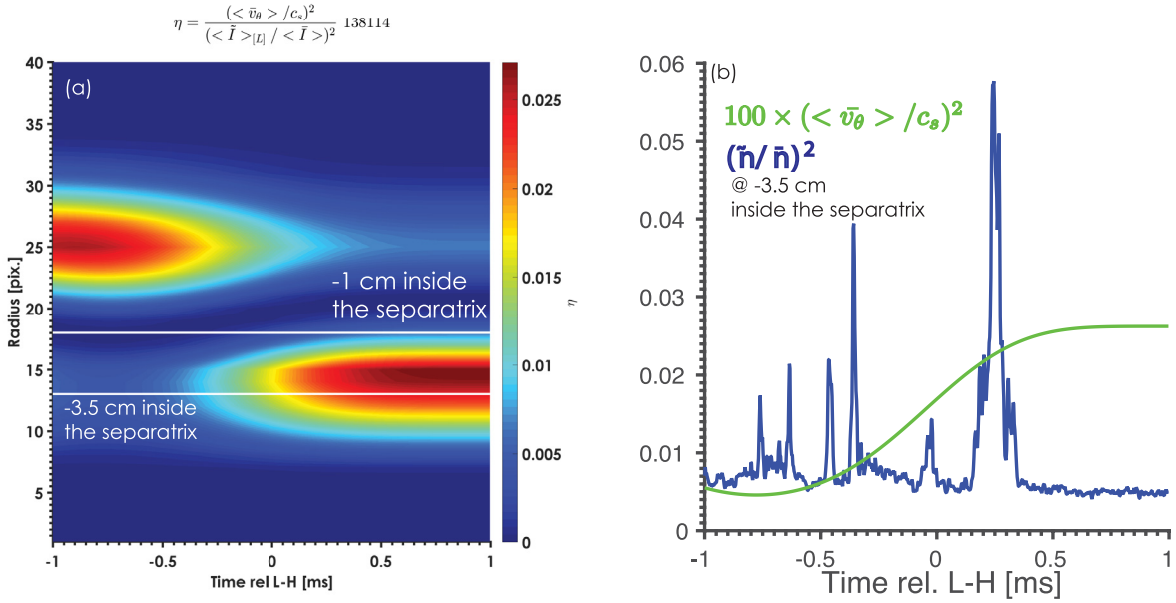

Figure 9. NBI case. Energy ratio of the kinetic energy to the thermal free energy. (*a*) Radial profile as a function of time relative to the L–H transition. (*b*) Time history at 3.5 cm inside the separatrix of the thermal free energy and 100 times the kinetic energy.

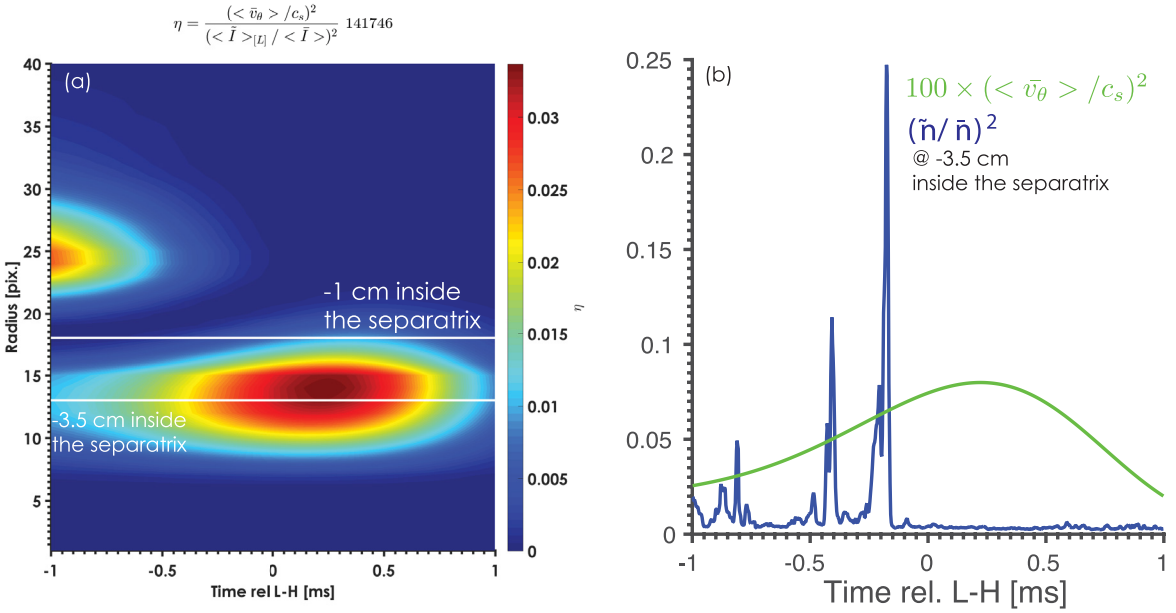

Figure 10. Ohmic case. Energy ratio of the kinetic energy to the free thermal energy. See figure 9 captions.

by direct energy transfer into the mean flow is an unlikely mechanism for the L–H transition.

Can the Reynolds stress contribute, however, to the mean flow itself? Here, we estimate the Reynolds-stress-driven flow and compare it to the measured mean flows. Under the assumptions highlighted in section 2, one can crudely estimate the contribution of the Reynolds stress to the poloidal flow by estimating from experimental data $\langle \tilde{v}_\theta \rangle^{\mathrm{RS}} \sim -qR\frac{\partial_r \langle \tilde{v}_\theta \tilde{v}_r \rangle}{v_{\mathrm{thi}}}$, where q is the safety factor, and v_{thi} is the ion thermal velocity.

Figure 13 displays the estimated Reynolds stress contribution to the mean poloidal flow at four radii, which is compared with the GPI measured mean poloidal flow. This figure shows that both the Reynolds stress-driven mean flow (red curve) and the measured mean flow (blue curve) are of the same order of magnitude. This suggests that the contribution of the Reynolds stress to the mean flow cannot necessarily be discarded. (This is not inconsistent with the fact that Reynolds work is unable to deplete the turbulence free energy, since the turbulence free energy is much larger than the kinetic energy of the mean poloidal flows.) Note that given how crudely we estimate the contribution of the Reynolds stress, it is difficult to claim any consistency better than an order of magnitude.

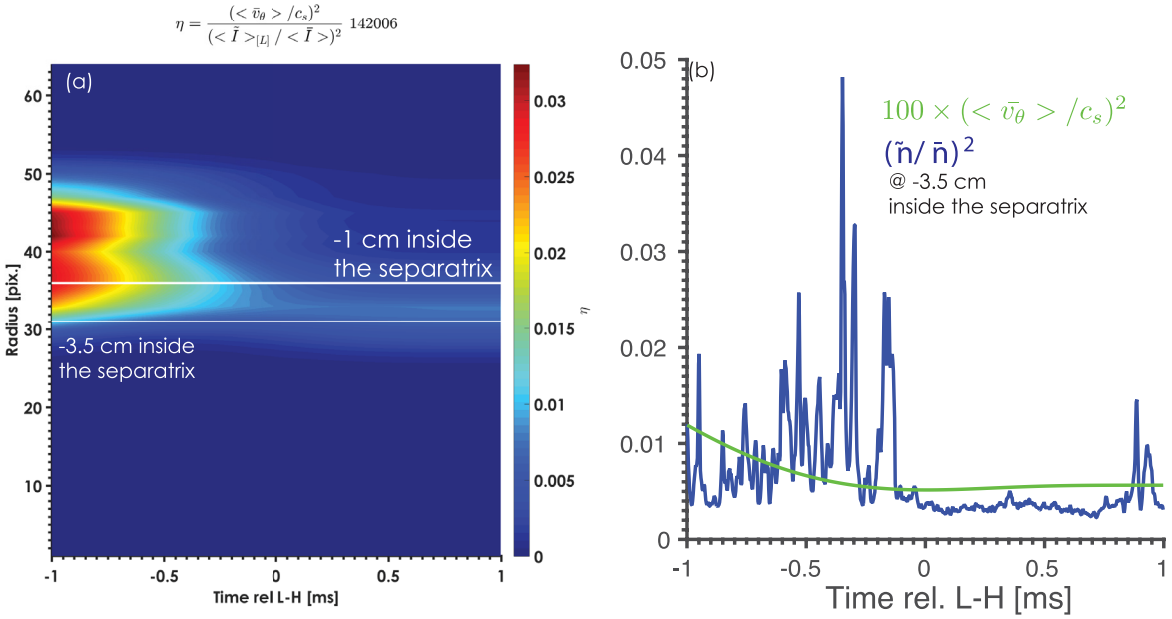

Figure 11. RF case. Energy ratio of the kinetic energy to the free thermal energy. See figure 9 captions. Here, the peak of the ratio appears to continuously move inward across the L–H transition.

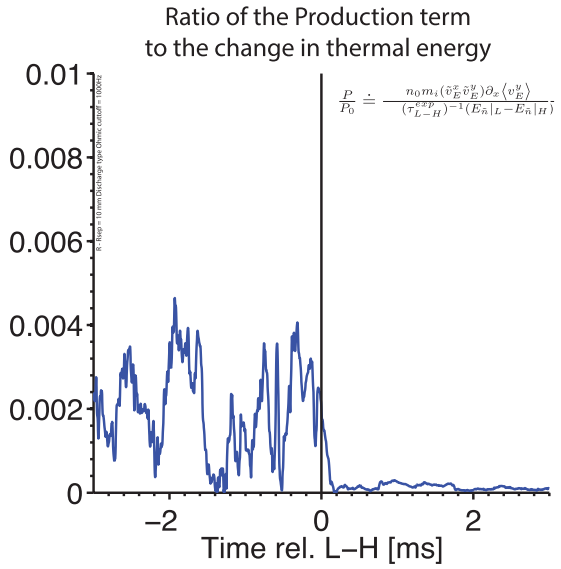

Figure 12. Ohmic case. Ratio of the Reynolds work to the change (in L & H modes) in thermal free energy (see text for discussion).

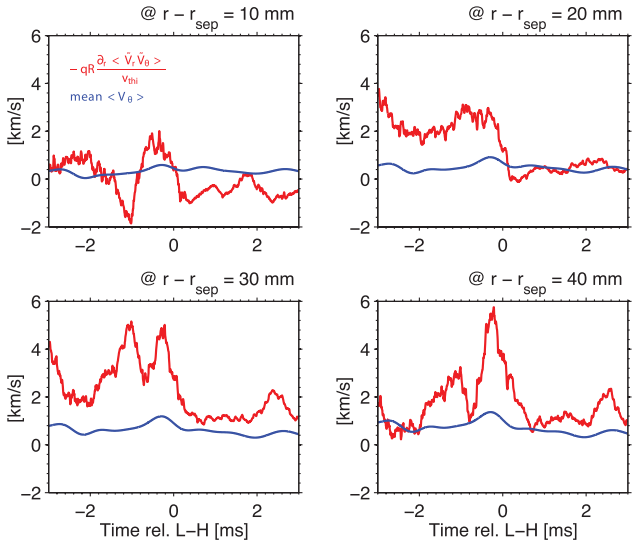

Figure 13. NBI case: the comparison at various radii between the measured mean flow to the estimated Reynolds stress-driven flow shows order of magnitude agreement (see text for discussion). Since the Reynolds stress estimate is only good to an order of magnitude, the error bars have not been included because they might only change the results within an order unity.

4. Summary

We described detailed analyses of the energy dynamics during the L–H transition in NSTX over a database of 17 discharges spanning three heating schemes (NBI, ohmic, and RF). These analyses utilized the GPI data for determining the velocity fields using the ODP velocimetry approach. We used a minimal model [11] of edge turbulence and sheared flows to describe the transfer of energy between turbulence and flows via the Reynolds stress in order to understand the L–H transition.

The analysis then proceeded to evaluate the energy exchange dynamics across the L–H transition. More specifically, we investigated the exchange dynamics on NSTX discharges, and the results can be summarized into three points.

- The relative GPI fluctuation decreased rapidly and consistently across the L–H transition, as shown in figures 1(*a*) and 2(*a*), which is consistent with many previous experimental results at the L–H transition. However, there were no consistent changes *preceding* the L–H transition in the relative fluctuation level, the average poloidal or radial correlation lengths, the average poloidal or radial velocities, or the average poloidal flow shear, as shown in figures 2(*b*), (*c*), 4, 6(*b*), 7(*b*), and 8(*b*). This absence of a precursor or 'trigger' signal preceding the transition is also a relatively common result, but is

shown here for NSTX in a clear way over a large database. Finally, these turbulence quantities do change from before to after the transition, as would be expected from the well-known edge profile changes, but this does not help to identify the L–H transition mechanism.

- We then proceeded to the examination of energy transfer via the Reynolds stress and production term. This analysis was performed using a newly implemented velocimetry approach (ODP) to obtain the radial and poloidal velocities with better temporal and spatial resolution than TDE. We use three approaches to examine the transfer dynamics.

  – We computed the production term in a region corresponding to the H-mode pedestal (1 cm inside the separatrix). We systematically inferred a negative production term, which suggests an energy transfer from mean flows to turbulence. The inferred sign is inconsistent with fluctuation level drops across the L–H transition and with the predator–prey model.
  – This discrepancy, along with the significant uncertainties inherent in the velocity analysis, motivated theoretical work [11]. The key aspect of this model is to include the parallel electron dynamics and the thermal free energy, consistent with the original predator–prey model [5]. The key result is that in order for Reynolds work to suppress the turbulence, it must deplete the total turbulent free energy, including the thermal free-energy term. For this to occur, the increase in kinetic energy in the mean flow over the L–H transition must be comparable to the pre-transition thermal free energy. However, this ratio was found to be of order 10^{-2}, even at its maximum (3.5 cm inside the LCFS). Although there are significant simplifications in the theoretical model, they are very unlikely to cause inaccuracy by two orders of magnitude, suggesting that direct turbulence depletion by the Reynolds work may not be large enough to explain the L–H transition on NSTX, contrary to the predator–prey model.
  – Finally, we examined the absolute value of the production term to assess its contribution to the duration of the L–H transition, and found that given our inferred absolute value of the production term, the L–H transition duration should be about 18 ms, which is far too long compared to the experimentally estimated duration of around 100μs. Alternatively, we computed the ratio of the Reynolds work to the change of thermal free energy, which was found to be much less than 1. Despite the uncertainty due to velocimetry and theoretical modeling, the very large discrepancy suggests that the production term cannot cause the change in thermal free energy on NSTX, as would be required for turbulence depletion.

- Nonnegligible contribution to the poloidal flows by the Reynolds stress, however, is plausible given the comparable magnitude of the measured mean poloidal flows with the estimated Reynolds-stress-driven flows.

In summary, this analysis suggests that turbulence depletion by Reynolds work is probably not the mechanism of the L–H transition in NSTX, but no alternative mechanism was found from either the experimental data or from the new model. However, there are still significant uncertainties in the analysis and interpretation of the 2D velocity fields derived from the GPI data, especially during the H-mode phase, which can be reduced with additional measurements and quantitative comparisons with turbulence simulations.

Acknowledgments

This work was supported by US Department of Energy Contract DE-AC02-09CH11466. Note that the digital data for this paper can be found at http://arks.princeton.edu/ark:/88435/dsp01f1881p40x.

References

[1] Wagner F. *et al* 1982 *Phys. Rev. Lett.* **49** 1408
[2] ASDEX Team 1989 *Nucl. Fusion* **29** 1959
[3] Burrell K.H. 1997 *Phys. Plasmas* **4** 1499
[4] Biglari H., Diamond P.H. and Terry P.W. 1990 *Phys. Fluids* B **2** 1
[5] Diamond P.H., Liang Y.-M., Carreras B.A. and Terry P.W. 1994 *Phys. Rev. Lett.* **72** 2565
[6] Xu G. *et al* 2014 *Nucl. Fusion* **54** 103002
[7] Yan Z. *et al* 2014 *Phys. Rev. Lett.* **112** 125002
[8] Cziegler I. *et al* 2014 *Plasma Phys. Control. Fusion* **56** 075013
[9] Xu M. *et al* 2012 *Phys. Rev. Lett.* **108** 245001
[10] Sánchez E. *et al* 2005 *J. Nucl. Mater.* **337–9** 296
[11] Stoltzfus-Dueck T. 2016 *Phys. Plasmas* **23** 054505
[12] Scott B.D. 2007 *Phys. Plasmas* **14** 102318
[13] Scott B. 2010 *Phys. Plasmas* **17** 102306
[14] Novakovskii S.V., Liu C.S., Sagdeev R.Z. and Rosenbluth M.N. 1997 *Phys. Plasmas* **4** 4272
[15] Scott B.D. 2005 *New J. Phys.* **7** 92
[16] Zweben S.J. *et al* 2006 *Phys. Plasmas* **13** 056114
[17] Zweben S. *et al* 2015 *Nucl. Fusion* **55** 093035
[18] Zweben S.J. *et al* 2010 *Phys. Plasmas* **17** 102502
[19] Sechrest Y. *et al* 2011 *Phys. Plasmas* **18** 012502
[20] McKee G.R. *et al* 2006 *Rev. Sci. Instrum.* **77** 10F104
[21] Hirsch M., Holzhauer E., Baldzuhn J., Kurzan B. and Scott B. 2001 *Plasma Phys. Control. Fusion* **43** 1641
[22] Myra J. *et al* 2013 *Nucl. Fusion* **53** 073013
[23] Sierchio J.M., Cziegler I., Terry J.L., White A.E. and Zweben S.J. 2016 *Rev. Sci. Instrum.* **87** 023502
[24] Banerjee S. *et al* 2015 *Rev. Sci. Instrum.* **86** 033505
[25] Diallo A. *et al* 2013 *Nucl. Fusion* **53** 093026